Research Article

Integrating Plasmonic Supercrystals in Microfluidics for Ultrasensitive, Label-Free, and Selective Surface-Enhanced Raman Spectroscopy Detection

Daniel García-Lojo,[¶] Sergio Gómez-Graña,[¶] Víctor F. Martín, Diego M. Solís, José M. Taboada, Jorge Pérez-Juste,* and Isabel Pastoriza-Santos*

Cite This: *ACS Appl. Mater. Interfaces* 2020, 12, 46557−46564

Read Online

ACCESS | 📊 Metrics & More | 📰 Article Recommendations | 🆘 Supporting Information

ABSTRACT: Surface-enhanced Raman spectroscopy (SERS) microfluidic chips for label-free and ultrasensitive detection are fabricated by integrating a plasmonic supercrystal within microfluidic channels. This plasmonic platform allows the uniform infiltration of the analytes within the supercrystal, reaching the so-called hot spots. Moreover, state-of-the-art simulations performed using large-scale supercrystal models demonstrate that the excellent SERS response is due to the hierarchical nanoparticle organization, the interparticle separation (IPS), and the presence of supercrystal defects. Proof-of-concept experiments confirm the outstanding performance of the microfluidic chips for the ultradetection of (bio)molecules with no metal affinity. In fact, a limit of detection (LOD) as low as 10^{-19} M was reached for crystal violet. The SERS microfluidic chips show excellent sensitivity in the direct analysis of pyocyanin secreted by *Pseudomonas aeruginosa* grown in a liquid culture medium. Finally, the further integration of a silica-based column in the plasmonic microchip provides charge-selective SERS capabilities as demonstrated for a mixture of positively and negatively charged molecules.

▷ SiO₂ assembly
▷ Selective charge filter
▷ Plasmonic supercrystal
▷ Antenna effect
▷ Label-free ultradetection

KEYWORDS: plasmonic supercrystals, microfluidics, SERS sensing, Au nanoparticles, microchromatography
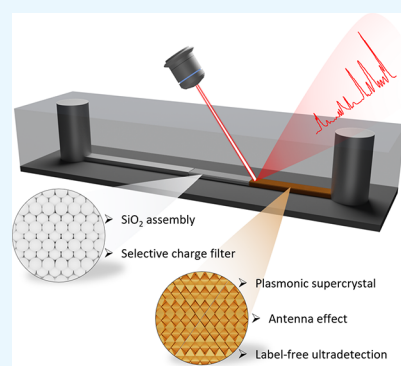
INTRODUCTION

Microfluidics is a multidisciplinary technology widely applied across many areas of science and technology over the last two decades.[1−3] In the field of (bio)sensing, microfluidics has enabled the miniaturization, parallelization, automation, and integration of (bio)chemical analysis, which has enormously benefited the sensor technology. Moreover, the merger of both technologies has evolved into a new generation of point-of-care (PoC) sensors with improved capabilities including through-put processing, higher sensitivity, and reliability, multiplexing, or real-time detection.[4,5]

Among the different chemical and biomolecular detection techniques (ref 6 and references therein), surface-enhanced Raman spectroscopy (SERS)-based sensing has emerged as a promising alternative to overcome some of the limitations shown by the typical ultrasensitive techniques (time-consuming, expensive, and long sample preparation processes).[7−9] Apart from that, SERS shows other advantages such as multiplex label-free detection, high sensitivity, and extremely high spectral selectivity.[10] Focusing on sensitivity and reliability, the performance of a SERS sensor is strongly dependent on the intensity and uniformity of the electric near-field enhancement generated by the plasmonic nanostructure used to amplify the Raman signal of the molecule of interest. Taking into account that the SERS intensity is related to the number of hot spots per illumination volume, the most efficient plasmonic substrates would be 3D plasmonic supercrystals.[11,12] Recent simulations performed with densely packed gold nanorod arrays demonstrated higher SERS enhancement when the crystalline order was imposed on the nanoparticle assembly.[13]

When comparing with randomly distributed nanorods, the SERS intensities are much larger and uniform in the case of a periodic arrangement of Au nanoparticles because it generates confined propagation modes, producing strong hot spots distributed at different resonant depths of the whole ordered nanostructure. In spite of the higher SERS efficiency of plasmonic supercrystals, just a few reports have been published on their use for SERS-based sensing.[14] As recently reviewed, different strategies can be employed to fabricate highly ordered 3D plasmonic nanostructures comprising Au and Ag nanoparticles.[14] Among them, the drop-casting technique is arguably the most widely used although its applicability is
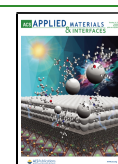
limited, in part, because of the lack of reproducibility in the supercrystal fabrication and the small area/volume of the assemblies.[15,16] The process involves the evaporation-induced self-assembly controlled by different kinetic and thermodynamic factors. Recently, the stamping technique has intensely emerged as an alternative tool to solve the reproducibility issues, fabricating highly ordered plasmonic platforms with reliable SERS performance,[17,18] although the supercrystal dimensions obtained via stamping are limited to a few microns. Another important issue is the location of the analyte in the inner gaps and planes because this methodology does not favor the analyte infiltration.

Likewise, during the last years, microfluidic devices have arisen as promising new systems to create 3D materials based on self-assembled nanoparticles with tailored size and shape.[19] Taking advantage of this new microfluidic pervaporators, we have recently fabricated plasmonic supercrystals using microfluidic-assisted assembly. Besides, we demonstrated that these 3D plasmonic assemblies can act as highly reliable and sensitive SERS sensing platforms.[20]

Based on the knowledge gained in constructing plasmonic supercrystals inside microfluidic channels, herein, we go a step further designing a SERS-based microfluidic chip for analyte detection, which combines the high sensitivity and label-free analysis of the plasmonic supercrystals with the advantages of microfluidics such as portability for PoC detection, high-throughput low sample consumption, and ease of being integrated into an array format (see Scheme 1). Moreover, we

Scheme 1. Schematic Representation of the Fabrication of the Plasmonic Supercrystal Microchip. (A) Injection of a Colloidal Dispersion of Gold Nanooctahedrons and Pervaporation-Induced Assembly of the Nanoparticles. (B) Plasmonic Supercrystal Chip after Punching an Outlet at the End of the Microchannel
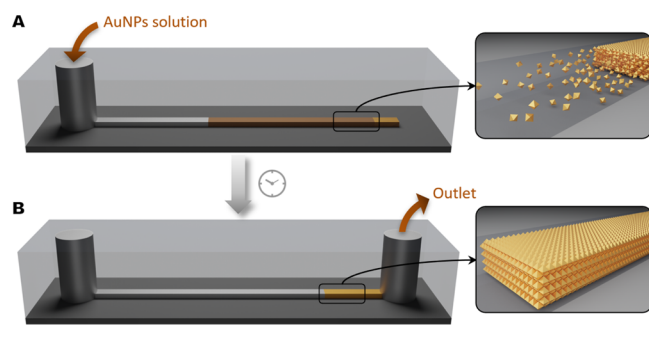
demonstrate that the integration of the SERS platform within the microfluidic system allows the infiltration and detection of analytes in flow (independently of its affinity toward the gold surface) even below the zeptomolar regime. We also carry out state-of-the-art SERS simulations using a large-scale supercrystal model with more than 8000 Au nanoparticles using the M^3 frequency domain full-wave solver, which is a highly scalable parallel implementation of the surface integral equation–domain decomposition method. It allows us to investigate the effect of the interparticle separation (IPS) and disorder in the SERS activity within the supercrystal. Finally, we investigate the incorporation of a silica-based chromatographic unit in the plasmonic microfluidic chip in order to provide charge selectively.

RESULTS AND DISCUSSION

A poly(dimethylsiloxane) (PDMS) microfluidic chip consisting of an end-closed microchannel (2 cm length; 50 μm width; and 12 μm height) with an inlet was fabricated using standard soft photolithography (see the experimental section for details, Scheme S1, and Figure S1, Supporting Information). The integration of a SERS active component in the microfluidic chip was performed by microfluidic-induced assembly of monodispersed gold nano-octahedrons within the channel, as previously described with some modifications.[20] Cetyltrimethylammonium bromide (CTAB)-stabilized Au octahedrons (75 nm side length) were selected as building blocks because previous analysis demonstrated their high SERS capabilities with thiolated molecules when forming supercrystals. Au octahedrons were synthesized by the overgrowth of Au nanorods (seeds) through the reduction of $AuCl_4^-$ with 3-butenoic acid (see experimental section and Figure S2, Supporting Information).[20] After adjusting the Au and CTAB concentrations to 200 and 0.1 mM, respectively, the microchannels were filled. Thus, around 10 μL of Au colloids was introduced in the inlet and induced to flow inside the microchannel by applying controlled pressure cycles (Figure S3, Supporting Information). The gradual evaporation of the solvent, occurring through the thinner PDMS film, generates a compensation flux that drives Au nanoparticles toward the end of the channel[19] and eventually their assembly into a 3D supercrystal. The resulting 3D self-assembly was characterized by scanning electron microscopy (SEM) characterization after peeling off the PDMS film. As shown in Figures 1A,B and S4A
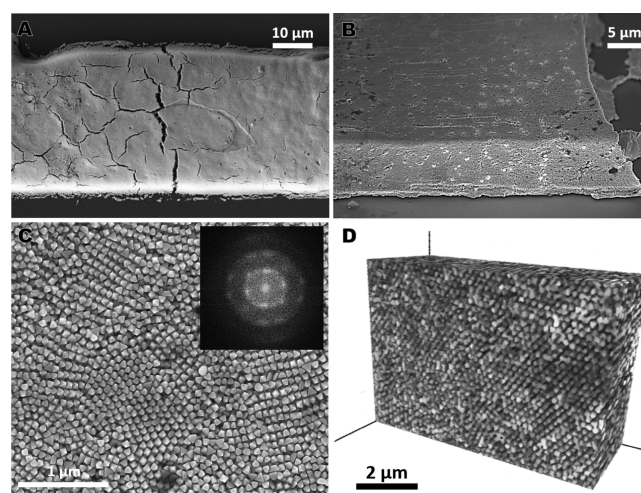

Figure 1. Au supercrystal characterization by SEM and FIB−SEM. (A−C) SEM images of an Au supercrystal at different magnifications. (A,C) are top views, while the image in (B) was acquired with a tilting angle of 52°. The inset in (C) shows the Fourier transform obtained from the same image. (D) 3D reconstruction of an Au supercrystal block (volume of 8 μm^3).

(Supporting Information), the particle assembly resembles the channel shape and dimensions. SEM analysis also evidences the hierarchical Au organization to form a densely close-packed supercrystal of gold octahedrons (Figures 1C, S4, and S5, Supporting Information). Besides, the Fourier transform pattern obtained from the analysis of SEM images also indicates local crystal order (inset in Figure 1C). To further investigate the internal structure of the Au supercrystals, we perform 3D reconstruction of the Au supercrystal block. In

order to do this, first, the sequential milling with a focused ion beam (FIB) of an Au supercrystal slice and SEM imaging of the exposed block cross-section (Figure S4, Supporting Information) are carried out. Finally, the 3D reconstruction of the Au supercrystal slice from the 2D SEM micrographs by means of the Slice & View method was performed. The 3D reconstruction (Figure 1D) and the 2D cross-section images (Figure S4 and Movie S1 for 3D reconstruction of the supercrystals, Supporting Information) indicate an internal organization of the Au octahedrons with areas with local hexagonal ordering.

After the integration of the supercrystal within the microfluidic system, an outlet at the end of the channel was opened to obtain the final chip configuration shown in Scheme 1. Next, the evaluation of the plasmonic microfluidic chip (noted as the plasmonic microchip) for SERS sensing was performed. We started by analyzing the ability of molecules to diffuse/infiltrate within the supercrystals and to reach the internal hot spots because it will determine the Raman enhancing capability of the microchip. As reported in supercrystals, high SERS enhancement is produced over extensive regions because of internal antenna effects.[13] For the molecular infiltration analysis, we chose a model Raman active molecule 1-naphthalenethiol (1-NAT), which exhibits a high affinity for Au.[21] Thus, 10 μL of 10^{-5} M 1-NAT was injected in the microchip and pumped at 250 mbar for 30 min, and then, the SERS spectrum was recorded using a 785 nm excitation laser line. As shown in Figure 2A the SERS spectrum exhibits the characteristic vibrational peaks of 1-NAT, including the peaks assigned to ring stretching (1369, 1501, and 1555 cm^{-1}), ring breathing (818 and 964 cm^{-1}), ring deformation (514, 536, and 660 cm^{-1}), C−S stretching (396 cm^{-1}), and C−H bending (1196 cm^{-1}).[22] Moreover, we performed 3D SERS analysis to investigate the spatial distribution of 1-NAT in the plasmonic supercrystal, which allowed us to evaluate the average SERS intensity. Thus, a depth profile analysis was first carried out by recording SERS spectra from 40 to −40 μm of the optical focus every 1 μm through the plasmonic microchip. Figure 2B shows the SERS intensity depth profile obtained by selecting the SERS signal to baseline from 1340 to 1390 cm^{-1}. The profile shows a maximum intensity plateau of around 12 μm thick, which corresponds with the height of the microfluidic channel (Figure S1, Supporting Information) and therefore with the height of the supercrystal. It demonstrates the 1-NAT infiltration through the supercrystal. Following a similar strategy, SERS intensity mappings were recorded at a different depth from 20 to −20 μm of the optical focus with a 4 μm step size. Figure 2C shows the SERS maps at different depths (see the color code in Figure 2B and SERS analysis in the Supporting Information where the z-resolution is described); the high uniformity in the SERS signal observed at the points located at the plateau, that is, at the supercrystal should be noted. These results confirm the uniform analyte diffusion into the supercrystal and the uniform distribution of hot spots. The tremendous advantage of this system relies on the possibility of infiltration of any kind of molecules, even molecules without gold affinity.

To better understand the SERS capability of the super-crystal, we computationally calculated the near-electric field distribution by means of electromagnetic simulations using the M^3 full-wave solver.[13,23] SERS enhancement is closely related to the near electromagnetic field and is often approximated by
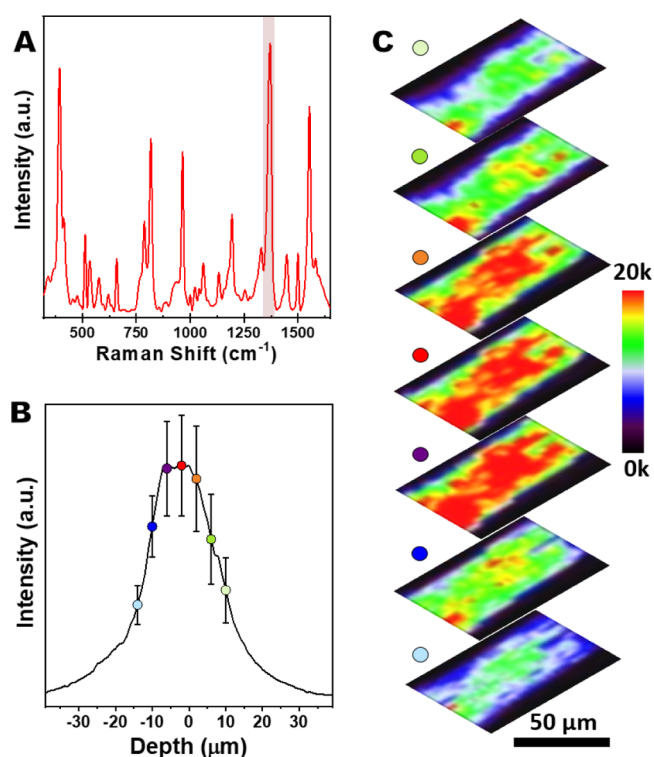

Figure 2. SERS analysis of the plasmonic microfluidic chip (A) Representative SERS spectrum of 1-naphthalenethiol. (B) SERS intensity depth profile recorded at 1369 cm^{-1} from 40 to −40 μm of the optical focus every 1 μm. Error bars represent the standard deviation from the SERS intensity maps in (C). (C) SERS intensity maps recorded by selecting the SERS signal to baseline from 1340 to 1390 cm^{-1} at different depths with a step of 4 μm. All measurements were recorded with a 785 nm laser line, 1.74 mW, 10 s acquisition time, and 1 accumulation.

averaging $|E/E_{inc}|^4$ over the number of molecules, with E_{inc} being the incident electric field and E being the near electric field.

The simulations were performed using as model a 3D assembly of 8200 octahedrons (75 nm side length), forming a perfect supercrystal of ca. 1 μm × 1 μm x 1.4 μm (length × width × height), see Figure 3A, for different IPSs (ranging from 1 to 4.5 nm, see cross-section models in Figures 3 and S6 in the Supporting Information). The results showed that the penetration of the incident light (the excitation laser line being 785 nm) is strongly dependent on the IPS. Thus, for 1 nm IPS, the near electric field is mainly located in the first layers of nanoparticles (Figure S6, Supporting Information) because the incident electromagnetic field is not able to penetrate inside the supercrystal because of the small IPS. This phenomenon, known as the cutting effect, comes up when the incident light frequency is above the cut-off frequency, which causes the scattering of the incident light. The cut-off frequency of a waveguide is the frequency above which signals will propagate through it with minimal attenuation. It depends on the shape and size of the cross-section of the waveguide, which, in our case, is defined by interparticle spaces. The larger the waveguide, the lower its cut-off frequency. This means that signals with a frequency above the cut-off frequency will propagate through a waveguide and signals below this frequency will be attenuated. It could be prevented by either increasing the light frequency over the cut-off frequency
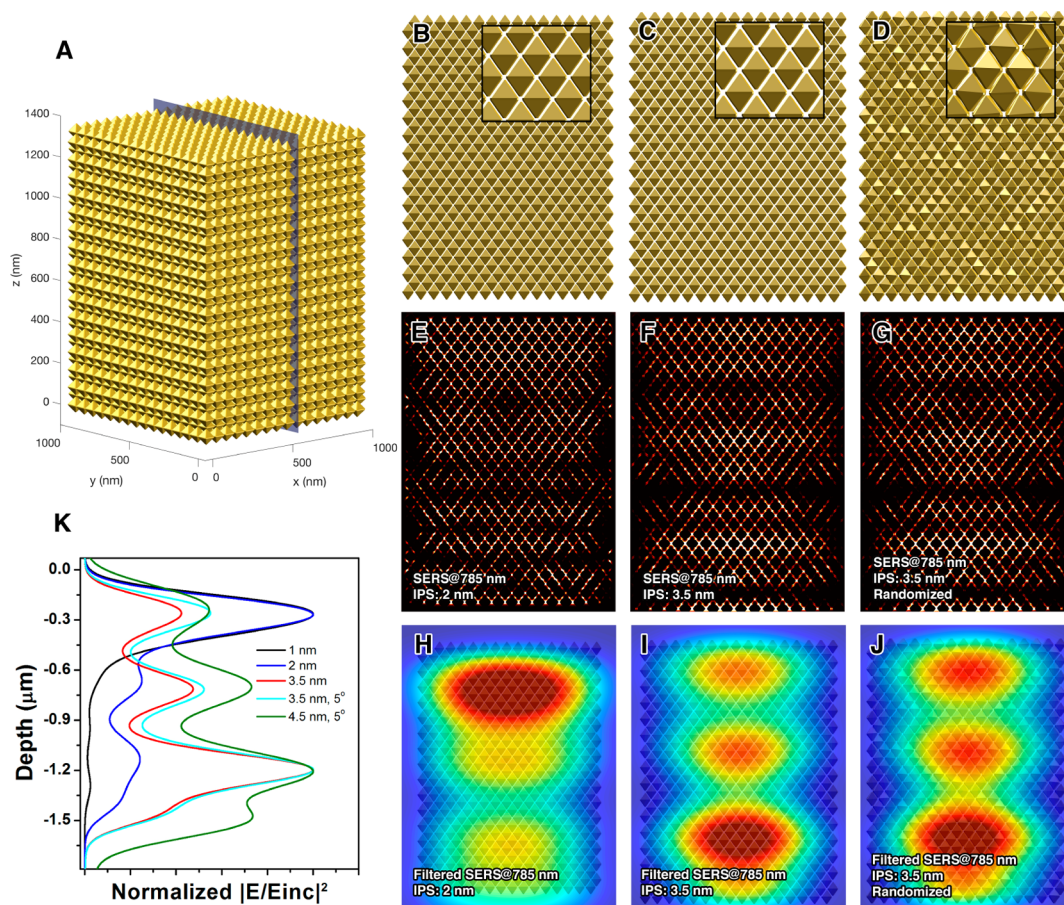
Figure 3. Electromagnetic simulations using the M^3 full-wave solver. (A) 3D supercrystal model of 8200 octahedrons (75 nm side length) compacted in a volume of ca. $1 \times 1 \times 1.4~\mu m^3$. (B–D) Cross-section of the supercrystal model showed in (A) with a surface-to-surface IPS of 2 (B), 3.5 (C), and 3.5 nm with $\pm 5°$ randomized in orientation (D). (E–G) SERS enhancement maps calculated in the plane x marked in A for the supercrystal for a IPS of 2 (E), 3.5 (F), and 3.5 nm with $\pm 5°$ randomized in orientation (G). (H–J) Filtered SERS enhancement maps obtained from (E–G) after convolution with a 2D Gaussian profile (to emulate a numerical aperture of 0.75, which corresponds with a spot size of 1.4 μm). (K) Normalized SERS enhancement on a line along the supercrystal axis for the different simulations described above.

(which can strongly affect the intensity of the near electromagnetic field generated in the supercrystal) or increasing the nanoparticle separation, which decreases the cut-off frequency. The latter is evidenced in the simulations performed at 2 and 3.5 nm IPS (Figure 3E,H for 2 nm and Figure 3F,I for 3.5 nm) where there is a higher penetration of the incident light as evidenced by the corresponding near-electric field distributions. Figure 3H,I correspond to simulations performed with Gaussian filtering for 2 and 3.5 nm supercrystal models, respectively. The Gaussian filtering allows us to include the effect of the receiving lens. Importantly, although the electric field distribution calculated for the 2 nm IPS model shows higher intensities close to the upper supercrystal surface (irradiation), 3.5 and 4.5 nm models evidence the presence of an electromagnetic standing wave along the 3D supercrystal being the most intense electric fields located at the bottom of the supercrystal. The differences in the electric field distribution with the distance can be easily observed in Figure 3K, where the field intensity is represented with the penetration depth. Taking into account that Au octahedrons are stabilized by a CTAB bilayer and that CTAB-stabilized Au nanoparticles assemblies show a IPS of approximately 3 nm,[24,25] it would explain, in part, the fact that we observed a continuous SERS signal along the z-axis of the substrate. Nevertheless, we did not observe the same intensity profile

(electromagnetic standing wave) probably because of the fact that the Au octahedron assemblies are nonperfect supercrystals (see Figures 1, S4, and S5, Supporting Information) presenting defects and rotations. In fact, introducing in the supercrystal model a small nanoparticle rotation of $\pm 5°$ in a random direction (see Figure 3D), the standing wave is smoothed, observing a more homogeneous electromagnetic field distribution inside the supercrystal (Figure 3K). Therefore, we believe that the uniform SERS intensities observed when analyzing the 1-NAT diffusion (Figure 2B,C) are the consequence of the IPS (around 3 nm) and the presence of small defects and low-range disorder within the Au assembly.

The SERS sensing capability of the plasmonic microchip was tested using as Raman probe crystal violet (CV), which has no covalent affinity for gold. First, the SERS response of the plasmonic microchip as a function of the infiltration time was investigated for 10^{-7} M CV injected at a 250 mbar constant pressure. SERS mappings and spectra recorded as a function of time showed the progressive CV diffusion and accumulation within the supercrystal with time (Figure S7). Then, the 3D spatial distribution of CV into the supercrystal was studied, observing a similar infiltration pattern as 1-NAT (Figure S8). Additionally, we analyzed the ability of the sensor to detect CV from concentration ranging from 10^{-7} to 10^{-15} M. The experiment was performed by injecting 60 μL of CV solution

at 250 mbar constant pressure for 30 min, that is, with a flow rate of 2 μL/min. The SERS analysis was performed by recording the SERS signal to baseline (from 1605 to 1630 cm^{-1}) intensity maps of CV (785 nm, 1.74 mW, 1 s, and five accumulations, Figure 4A). Thus, from the SERS intensity map
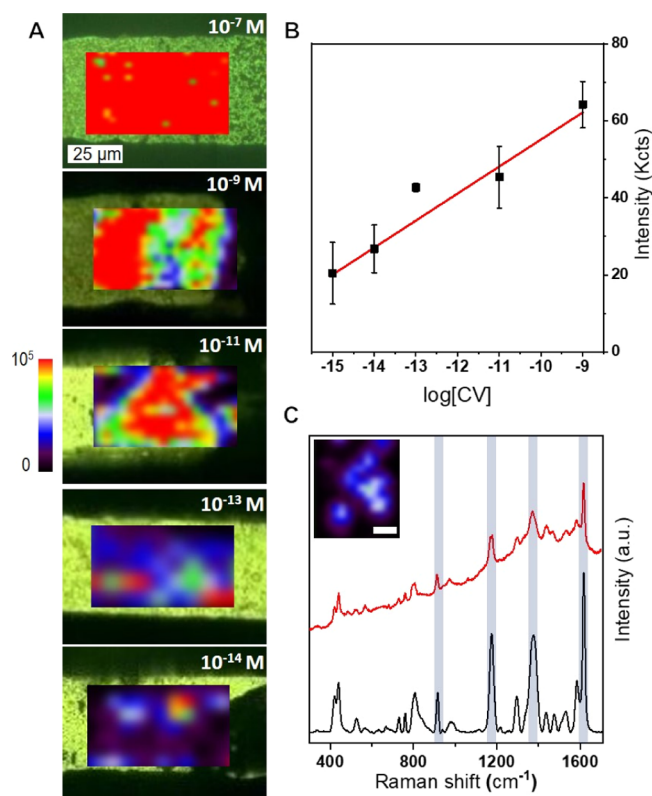

Figure 4. Analysis of the SERS sensing capabilities. (A) SERS intensity maps recorded by signal to baseline, between 1605 and 1630 cm^{-1}, for different CV concentrations, as indicated (785 nm laser line, 1.74 mW, 1 s, and five accumulations). (B) Average SERS intensity as a function of CV concentration. (C) SERRS spectrum recorded for a sample containing 10^{-19} M CV after 24 h of continuous infiltration (red) and representative SERRS spectrum of CV (black) for comparison. The inset shows the corresponding SERRS intensity map (the scale bar is 25 μm).

recorded at 10^{-7} M CV, a very uniform SERS signal is evidenced, in terms of signal and intensity, in the whole analyzed area, indicating both the homogeneous distribution of the analyte and more importantly the high quality of the supercrystal. The uniformity of the SERS signals and the average intensity progressively decrease with the CV concentrations (Figure 4B). Moreover, the analysis of the SERS data revealed that the average SERS intensity showed a linear dependence with the CV concentration from 10^{-9} to 10^{-15} M (Figure 4A). As shown in Figures S9 and S10 in the Supporting Information, the characteristic vibrational peaks of CV can be distinguished up to 10^{-15} M with no interference of the substrate (PDMS or CTAB). It should be noted that although CV has no covalent affinity for gold, the presence of CTAB molecules on the surface of the particles could promote its unspecific adsorption or retention, thus favoring its accumulation on the assembly. Importantly, the detection limit of the plasmonic microfluidic chip can be improved by working under resonant Raman conditions (laser line 633 nm for CV) and increasing the infiltration time. Thus, CV at a

concentration as low as 10^{-19} M was detected using longer infiltration time and increasing the flow rate (10 μL/min during 24 h) and 633 nm as the excitation laser line, as shown in the SERRS (surface-enhanced resonance Raman scattering) spectra and intensity map in Figure 4C. It should be noted that, to the best of our knowledge, such a low detection limit has not been reported before for CV.[26,27] It should be pointed out that the LOD and the experimental conditions needed to achieve it will strongly depend on the target molecule.

Once the ultradetection capabilities of the plasmonic microfluidic chip were demonstrated with CV, the next step was to test its performance with a real sample. Thus, the detection of pyocyanine produced in a *Pseudomonas aeruginosa* (*P. aeruginosa*) culture without the need for its extraction was investigated. Pyocyanin is an exclusive biomarker of this prevalent and opportunistic pathogen causing numerous human infections.[28] Moreover, direct and sensitive detection of pyocyanin in complex biological environments is still a challenge. In order to prove the suitability of the plasmonic microfluidic chips to detect pyocyanin avoiding the commonly used extraction processes involving organic solvents, a *P. aeruginosa* culture grown for 16 h (see the experimental section for details, Supporting Information) was centrifuged and after filtering the supernatant using an Amicon centrifugal filters (to separate large molecular weight proteins), it was injected inside the chip and analyzed by SERS. The concentration of the metabolite secreted by *P. aeruginosa* in the liquid culture was parallelly estimated by UV–vis spectroscopy at 691 nm (λ_{max} of pyocyanin) followed by chloroform extraction.[29] Figure 5A shows SERS spectra recorded from cultures at different dilutions where the characteristic peaks from pyocyanin (593, 633, 675, 1356, 1606, and 1619 cm^{-1})[30] were evidenced up to a concentration of 8 10^{-10} M. Figure 5B shows the SERS intensity map of pyocyanin at 8 10^{-9} M recorded by signal to baseline from 1340 to 1360 cm^{-1}. Therefore, these results demonstrated the better sensitivity of this methodology to detect pyocyanin at a nanomolar level in real samples versus the conventional UV–vis spectroscopy (suitable up to micromolar concentrations).

The possibility of integrating a chromatographic unit in the plasmonic microchip was investigated with the aim of providing charge selectivity and therefore improving its sensing capabilities.[31] Thus, silica particles of ca. 1 μm in diameter were assembled within the plasmonic microchip (see the scheme in Figure 6A) in a similar fashion as for the Au nanoparticles. Moreover, in order to fabricate two different SERS sensors, one selective for negatively charged molecules and another for positively charged ones, negatively or positively charged silica particles were integrated into the plasmonic microfluidic chip (see the experimental part for details, Supporting Information). Figure S11, Supporting Information, shows the SEM characterization of the silica–gold supercrystals after peeling off the PDMS film. We hypothesized that the silica nanoparticles within the microfluidic channel would produce a differential retention when a mixture of two oppositely charged molecules is introduced. It allowed the electrostatic-based separation of both components before reaching the plasmonic supercrystal for SERS detection.

The selectivity of both microfluidic sensors was tested employing CV and Acid Blue 25 (AB) as model analytes because they present positive- and negative-charged functional groups, respectively (Figure 6B). Importantly, the character- istic SERS features of both molecules (see Figure 6C) allow
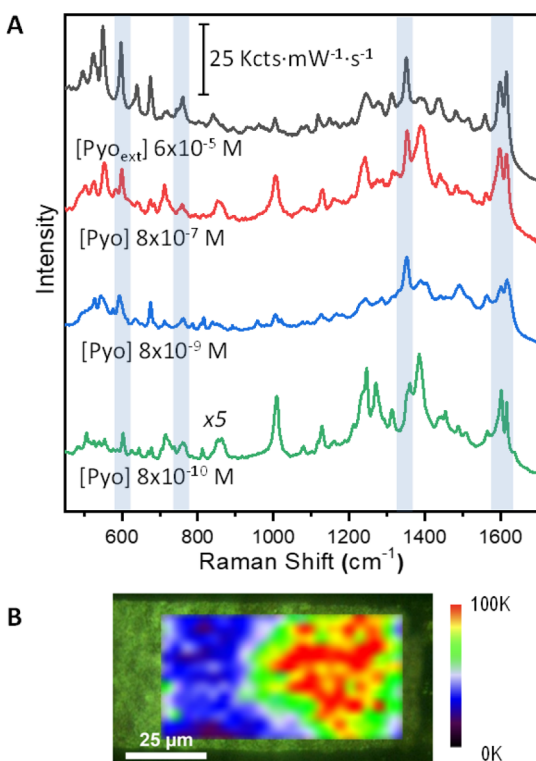
Figure 5. SERS analysis of pyocyanin produced in *P. aeruginosa* culture. (A) SERS spectra recorded from samples with different concentrations of pyocyanin (ranging from 8×10^{-7} to 8×10^{-10} M) obtained from a *P. aeruginosa* culture. Experimental conditions: 785 nm laser line, 0.256 mW, 10 s, and two accumulations. (B) Optical image of a plasmonic microfluidic channel and the optical image merged with the SERS intensity map of pyocyanin recorded by signal to baseline from 1340 to 1360 cm^{-1}. 785 nm laser line, 0.497 mW, 1 s, and two accumulations.

distinguishing them when mixed. In fact, if a sample containing both analytes (CV and AB) at 10^{-7} M concentration was injected in a plasmonic microfluidic chip without silica particles, no molecular selectivity was observed. Figure 6D shows SERS intensity maps recorded at a signal to baseline of 1265−1275 cm^{-1} (top) and 1615−1625 cm^{-1} (bottom) to visualize the spatial distribution of AB and CV, respectively. The mappings show a uniform distribution of both analytes along the supercrystal. The simultaneous detection of both analytes by the plasmonic microchip is also evidenced in the representative SERS spectrum (black) recorded during the analysis of the mixture.

Once we demonstrated that it is possible to distinguish both analytes when mixed, we tested the molecular selectivity of the plasmonic sensor toward negatively charged molecules, that is, AB. Again, a mixture of 10^{-7} M CV and 10^{-7} M AB was injected in the microchip, and after 30 min, the plasmonic microchip was analyzed by SERS. As mentioned above, the SERS intensity maps (Figure 6E) were recorded at a signal to baseline of 1265−1275 cm^{-1} (top) and 1615−1625 cm^{-1} (bottom) to visualize the spatial distribution of AB and CV, respectively. As shown in Figure 6E, the sensor is able to detect selectively AB. It is also evidenced in the representative SERS spectrum showed in Figure 6G (blue) where only the characteristic features of AB are distinguished.

This behavior could be explained considering that CV presented a higher retention time on the negatively charged
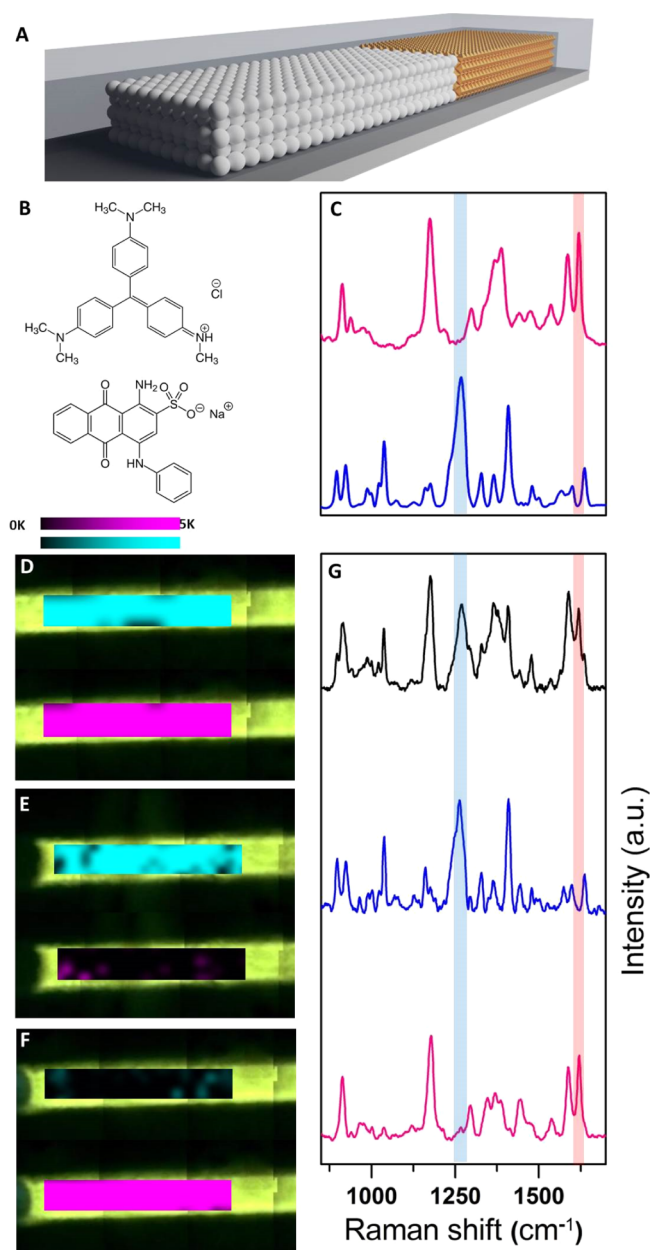

Figure 6. (A) Scheme of the charge-selective SERS microfluidic sensor which integrates a plasmonic component (Au supercrystal) and molecular trapping component (silica nanoparticles assembly) within a microfluidic channel. (B) Structures of CV and Acid Blue 25 (AB). (C) Representative SERS spectra of CV (magenta) and AB (blue) recorded with 785 nm laser line, 0.256 mW, 10 s, and two accumulations. (D−F) SERS intensity maps recorded at a signal to baseline of 1265−1275 cm^{-1} (top, CV) and 1615−1625 cm^{-1} (bottom, AB) after injection of a sample containing 10^{-7} M CV and 10^{-7} M AB in a nonselective (D), negative-charge-selective (E) and positive-charge-selective (F) plasmonic microchips. SERS mappings were recorded using a 785 nm laser line, 1.74 mW maximum power, 1 s accumulation time, and three accumulations. (G) Representative SERS spectra recorded in a nonselective (black), negative-charge-selective (blue), and positive-charge-selective (magenta) plasmonic microchips (785 nm laser line, 0.256 mW, maximum power, 10 s, and two accumulations).

silica nanoparticles preventing them from reaching the sensing area. In a similar way, a microfluidic sensor selective for positively charged molecules, that is, with positively charged

silica assembly was tested. Figure 6F shows the SERS analysis after the injection of a mixture of AB and CV. No significant SERS signals from AB in the plasmonic platform were observed, which indicated the selective detection of CV probably becausse of the larger retention time of AB molecules induced by the positively charged silica particles. Therefore, this proof of concept demonstrated the ability of the plasmonic microfluidic microchips in charge-selective molecule sensing.

CONCLUSIONS

In summary, we demonstrated that the integration of plasmonic supercrystals based on gold octahedrons within microfluidic channels allows the fabrication of plasmonic microchips with outstanding SERS performance for sensing. Thus, investigating the molecular diffusion in the supercrystal using 1-NAT (as a Raman probe), we found that (i) the molecule was uniformly infiltrated within the whole super-crystal and (ii) it exhibited an intense and highly uniform SERS response, which is due to a homogeneous distribution of hot spots. Realistic simulations performed with large-scale supercrystal models demonstrated that the experimentally observed SERS response with 1-NAT was due to IPS (given by the CTAB coating layer) and the presence of defects in the hierarchical nanoparticle organization. Besides, proof-of-concept experiments confirmed that the plasmonic microchips exhibit outstanding sensing performance for molecules with no affinity for the plasmonic surface (CV or pyocyanin), even when they are in biological complex media (such as bacteria culture for pyocyanin). In fact, a limit of detection (LOD) as low as 10^{-19} M was reached for CV and 10^{-9} M for pyocyanin released by *P. aeruginosa* in a liquid culture. Finally, we demonstrated that the further integration of a silica-based column in the plasmonic microchip provides charge-selective SERS capabilities in a mixture of positively and negatively charged molecules (CV and AB). To conclude, we have designed a plasmonic microchip with outstanding performance for ultratrace label-free SERS detection of analytes in low sample volumes, which also exhibits other advantages such as portability for PoC detection and high-throughput or easy manipulation.

ASSOCIATED CONTENT

Ⓢ Supporting Information

The Supporting Information is available free of charge at https://pubs.acs.org/doi/10.1021/acsami.0c13940.

    3D reconstruction of the supercrystals (MP4)

    Materials and methods, additional TEM and SEM images, and electromagnetic simulations (PDF)

AUTHOR INFORMATION

Corresponding Authors

Jorge Pérez-Juste − CINBIO, Universidade de Vigo, 36310 Vigo, Spain; Galicia Sur Health Research Institute (IIS Galicia Sur), SERGAS-UVIGO, 36310 Vigo, Spain; ⓞ orcid.org/ 0000-0002-4614-1699; Email: juste@uvigo.es

Isabel Pastoriza-Santos − CINBIO, Universidade de Vigo, 36310 Vigo, Spain; Galicia Sur Health Research Institute (IIS Galicia Sur), SERGAS-UVIGO, 36310 Vigo, Spain; ⓞ orcid.org/0000-0002-1091-1364; Email: pastoriza@ uvigo.es

Authors

Daniel García-Lojo − CINBIO, Universidade de Vigo, 36310 Vigo, Spain; Galicia Sur Health Research Institute (IIS Galicia Sur), SERGAS-UVIGO, 36310 Vigo, Spain

Sergio Gómez-Graña − CINBIO, Universidade de Vigo, 36310 Vigo, Spain; Galicia Sur Health Research Institute (IIS Galicia Sur), SERGAS-UVIGO, 36310 Vigo, Spain; ⓞ orcid.org/ 0000-0002-7736-051X

Víctor F. Martín − Departamento de Tecnología de Computadores y Comunicaciones, University of Extremadura, 10003 Cáceres, Spain; ⓞ orcid.org/0000-0001-7095-7148

Diego M. Solís − Departamento de Teoría de la Señal y Comunicaciones, Universidade de Vigo, 36310 Vigo, Spain

José M. Taboada − Departamento de Tecnologia de Computadores y Comunicaciones, University of Extremadura, 10003 Cáceres, Spain

Complete contact information is available at:
https://pubs.acs.org/10.1021/acsami.0c13940

Author Contributions

Notes

The authors declare no competing financial interest.

ACKNOWLEDGMENTS

REFERENCES

(1) Mark, D.; Haeberle, S.; Roth, G.; von Stetten, F.; Zengerle, R. Microfluidic lab-on-a-chip platforms: requirements, characteristics and applications. *Chem. Soc. Rev.* **2010**, *39*, 1153−1182.

(2) Sackmann, E. K.; Fulton, A. L.; Beebe, D. J. The present and future role of microfluidics in biomedical research. *Nature* **2014**, *507*, 181−189.

(3) Whitesides, G. M. The origins and the future of microfluidics. *Nature* **2006**, *442*, 368−373.

(4) Yan, W.; Yang, L.; Chen, J.; Wu, Y.; Wang, P.; Li, Z. In Situ Two-Step Photoreduced SERS Materials for On-Chip Single-Molecule Spectroscopy with High Reproducibility. *Adv. Mater.* **2017**, *29*, 1702893.

(5) Bai, S.; Serien, D.; Hu, A.; Sugioka, K. 3D Microfluidic Surface-Enhanced Raman Spectroscopy (SERS) Chips Fabricated by All-Femtosecond-Laser-Processing for Real-Time Sensing of Toxic Substances. *Adv. Funct. Mater.* **2018**, *28*, 1706262.

(6) Swager, T. M.; Mirica, K. A. Introduction: Chemical Sensors. *Chem. Rev.* **2019**, *119*, 1−2.

(7) Cialla-May, D.; Zheng, X.-S.; Weber, K.; Popp, J. Recent progress in surface-enhanced Raman spectroscopy for biological and biomedical applications: from cells to clinics. *Chem. Soc. Rev.* **2017**, *46*, 3945−3961.

(8) Alvarez-Puebla, R. A.; Liz-Marzán, L. M. SERS Detection of Small Inorganic Molecules and Ions. *Angew. Chem., Int. Ed.* **2012**, *51*, 11214−11223.

(9) Laing, S.; Gracie, K.; Faulds, K. Multiplex in vitro detection using SERS. *Chem. Soc. Rev.* **2016**, *45*, 1901−1918.

(10) Langer, J.; Jimenez de Aberasturi, D.; Aizpurua, J.; Alvarez-Puebla, R. A.; Auguié, B.; Baumberg, J. J.; Bazan, G. C.; Bell, S. E. J.; Boisen, A.; Brolo, A. G.; Choo, J.; Cialla-May, D.; Deckert, V.; Fabris, L.; Faulds, K.; García de Abajo, F. J.; Goodacre, R.; Graham, D.; Haes, A. J.; Haynes, C. L.; Huck, C.; Itoh, T.; Käll, M.; Kneipp, J.; Kotov, N. A.; Kuang, H.; Le Ru, E. C.; Lee, H. K.; Li, J.-F.; Ling, X. Y.; Maier, S. A.; Mayerhöfer, T.; Moskovits, M.; Murakoshi, K.; Nam, J.-M.; Nie, S.; Ozaki, Y.; Pastoriza-Santos, I.; Perez-Juste, J.; Popp, J.; Pucci, A.; Reich, S.; Ren, B.; Schatz, G. C.; Shegai, T.; Schlücker, S.; Tay, L.-L.; Thomas, K. G.; Tian, Z.-Q.; Van Duyne, R. P.; Vo-Dinh, T.; Wang, Y.; Willets, K. A.; Xu, C.; Xu, H.; Xu, Y.; Yamamoto, Y. S.; Zhao, B.; Liz-Marzán, L. M. Present and Future of Surface-Enhanced Raman Scattering. *ACS Nano* **2020**, *14*, 28−117.

(11) Alvarez-Puebla, R. A.; Agarwal, A.; Manna, P.; Khanal, B. P.; Aldeanueva-Potel, P.; Carbo-Argibay, E.; Pazos-Perez, N.; Vigderman, L.; Zubarev, E. R.; Kotov, N. A.; Liz-Marzan, L. M. Gold nanorods 3D-supercrystals as surface enhanced Raman scattering spectroscopy substrates for the rapid detection of scrambled prions. *Proc. Natl. Acad. Sci. U.S.A.* **2011**, *108*, 8157−8161.

(12) Hamon, C.; Novikov, S. M.; Scarabelli, L.; Solís, D. M.; Altantzis, T.; Bals, S.; Taboada, J. M.; Obelleiro, F.; Liz-Marzán, L. M. Collective Plasmonic Properties in Few-Layer Gold Nanorod Supercrystals. *ACS Photonics* **2015**, *2*, 1482−1488.

(13) Solís, D. M.; Taboada, J. M.; Obelleiro, F.; Liz-Marzán, L. M.; García de Abajo, F. J. Toward Ultimate Nanoplasmonics Modeling. *ACS Nano* **2014**, *8*, 7559−7570.

(14) García-Lojo, D.; Núñez-Sánchez, S.; Gómez-Graña, S.; Grzelczak, M.; Pastoriza-Santos, I.; Pérez-Juste, J.; Liz-Marzán, L. M. Plasmonic Supercrystals. *Acc. Chem. Res.* **2019**, *52*, 1855−1864.

(15) Gómez-Graña, S.; Pérez-Juste, J.; Alvarez-Puebla, R. A.; Guerrero-Martínez, A.; Liz-Marzán, L. M. Self-Assembly of Au@Ag Nanorods Mediated by Gemini Surfactants for Highly Efficient SERS-Active Supercrystals. *Adv. Opt. Mater.* **2013**, *1*, 477−481.

(16) Deng, K.; Luo, Z.; Tan, L.; Quan, Z. Self-assembly of anisotropic nanoparticles into functional superstructures. *Chem. Soc. Rev.* **2020**, *49*, 6002−6038.

(17) Matricardi, C.; Hanske, C.; Garcia-Pomar, J. L.; Langer, J.; Mihi, A.; Liz-Marzán, L. M. Gold Nanoparticle Plasmonic Superlattices as Surface-Enhanced Raman Spectroscopy Substrates. *ACS Nano* **2018**, *12*, 8531−8539.

(18) Hamon, C.; Sanz-Ortiz, M. N.; Modin, E.; Hill, E. H.; Scarabelli, L.; Chuvilin, A.; Liz-Marzán, L. M. Hierarchical organization and molecular diffusion in gold nanorod/silica supercrystal nanocomposites. *Nanoscale* **2016**, *8*, 7914−7922.

(19) Angly, J.; Iazzolino, A.; Salmon, J.-B.; Leng, J.; Chandran, S. P.; Ponsinet, V.; Désert, A.; Le Beulze, A.; Mornet, S.; Tréguer-Delapierre, M.; Correa-Duarte, M. A. Microfluidic-Induced Growth and Shape-Up of Three-Dimensional Extended Arrays of Densely Packed Nanoparticles. *ACS Nano* **2013**, *7*, 6465−6477.

(20) Gómez-Graña, S.; Fernández-López, C.; Polavarapu, L.; Salmon, J.-B.; Leng, J.; Pastoriza-Santos, I.; Pérez-Juste, J. Gold Nanooctahedra with Tunable Size and Microfluidic-Induced 3D Assembly for Highly Uniform SERS-Active Supercrystals. *Chem. Mater.* **2015**, *27*, 8310−8317.

(21) Alvarez-Puebla, R. A.; Dos Santos, D. S.; Aroca, R. F. Surface-enhanced Raman scattering for ultrasensitive chemical analysis of 1 and 2-naphthalenethiols. *Analyst* **2004**, *129*, 1251−1256.

(22) Zheng, G.; de Marchi, S.; López-Puente, V.; Sentosun, K.; Polavarapu, L.; Pérez-Juste, I.; Hill, E. H.; Bals, S.; Liz-Marzán, L. M.; Pastoriza-Santos, I.; Pérez-Juste, J. Encapsulation of Single Plasmonic Nanoparticles within ZIF-8 and SERS Analysis of the MOF Flexibility. *Small* **2016**, *12*, 3935−3943.

(23) Solís, D. M.; Taboada, J. M.; Obelleiro, F.; Liz-Marzán, L. M.; García de Abajo, F. J. Optimization of Nanoparticle-Based SERS Substrates through Large Scale Realistic Simulations. *ACS Photonics* **2017**, *4*, 329−337.

(24) Gómez-Graña, S.; Hubert, F.; Testard, F.; Guerrero-Martínez, A.; Grillo, I.; Liz-Marzán, L. M.; Spalla, O. Surfactant (Bi)Layers on Gold Nanorods. *Langmuir* **2012**, *28*, 1453−1459.

(25) Guerrero-Martínez, A.; Pérez-Juste, J.; Carbó-Argibay, E.; Tardajos, G.; Liz-Marzán, L. M. Gemini-Surfactant-Directed Self-Assembly of Monodisperse Gold Nanorods into Standing Super-lattices. *Angew. Chem., Int. Ed.* **2009**, *48*, 9484−9488.

(26) Fateixa, S.; Nogueira, H. I. S.; Trindade, T. Surface-Enhanced Raman Scattering Spectral Imaging for the Attomolar Range Detection of Crystal Violet in Contaminated Water. *ACS Omega* **2018**, *3*, 4331−4341.

(27) Chen, X.; Nguyen, T. H. D.; Gu, L.; Lin, M. Use of Standing Gold Nanorods for Detection of Malachite Green and Crystal Violet in Fish by SERS. *J. Food Sci.* **2017**, *82*, 1640−1646.

(28) Castillo-Juárez, I.; Maeda, T.; Mandujano-Tinoco, E. A.; Tomás, M.; Pérez-Eretza, B.; García-Contreras, S. J.; Wood, T. K.; García-Contreras, R. Role of quorum sensing in bacterial infections. *World J. Clin. Case* **2015**, *3*, 575−598.

(29) Reszka, K. J.; O'Malley, Y.; McCormick, M. L.; Denning, G. M.; Britigan, B. E. Oxidation of pyocyanin, a cytotoxic product from Pseudomonas aeruginosa, by microperoxidase 11 and hydrogen peroxide. *Free Radical Biol. Med.* **2004**, *36*, 1448−1459.

(30) Bodelón, G.; Montes-García, V.; López-Puente, V.; Hill, E. H.; Hamon, C.; Sanz-Ortiz, M. N.; Rodal-Cedeira, S.; Costas, C.; Celiksoy, S.; Pérez-Juste, I.; Scarabelli, L.; La Porta, A.; Pérez-Juste, J.; Pastoriza-Santos, I.; Liz-Marzán, L. M. Detection and imaging of quorum sensing in Pseudomonas aeruginosa biofilm communities by surface-enhanced resonance Raman scattering. *Nat. Mater.* **2016**, *15*, 1203−1211.

(31) Xia, Y.; Whitesides, G. M. Soft lithography. *Angew. Chem., Int. Ed.* **1998**, *37*, 550−575.